Journal of Catalysis 258 (2008) 235–242

Contents lists available at ScienceDirect

Journal of Catalysis

www.elsevier.com/locate/jcat

Investigation of CoS_2-based thin films as model catalysts for the oxygen reduction reaction

L. Zhu [a], D. Susac [a], M. Teo [a], K.C. Wong [a], P.C. Wong [a], R.R. Parsons [b], D. Bizzotto [a], K.A.R. Mitchell [a,*], S.A. Campbell [c,*]

[a] Department of Chemistry, University of British Columbia, 2036 Main Mall, Vancouver, British Columbia, Canada V6T 1Z1
[b] Department of Physics & Astronomy, University of British Columbia, 6224 Agricultural Road, Vancouver, British Columbia, Canada V6T 1Z1
[c] Ballard Power Systems Inc., 9000 Glenlyon Parkway, Burnaby, British Columbia, Canada V5J 5J9

ARTICLE INFO

Article history:
Received 10 March 2008
Revised 10 June 2008
Accepted 13 June 2008
Available online 14 July 2008

Keywords:
Transition metal sulfide
CoS_2
Proton exchange membrane fuel cell
Oxygen reduction reaction
Dynamic polarization
X-ray diffraction
Micro-Raman spectroscopy
Atomic force microscopy
X-ray photoelectron spectroscopy
Scanning Auger microscopy
Magnetron sputtering

ABSTRACT

Three CoS_2-, NiS_2- and $(Co,Ni)S_2$-based thin films were prepared by magnetron sputtering and studied as catalysts for the oxygen reduction reaction (ORR). Electrochemical assessments indicate that all three films have significant ORR catalytic activities, with that of $(Co,Ni)S_2$-type showing the best performance with regard to both open circuit potential (OCP) and current density. The ternary film has an OCP value of 0.89 V vs. the reversible hydrogen electrode, and shows a closer approach to values for Pt than have been obtained to date for other transition metal chalcogenides. The thin films assessed by electrochemistry have been characterized by a range of techniques including high-resolution X-ray diffraction, micro-Raman spectroscopy, atomic force microscopy, X-ray photoelectron spectroscopy and scanning Auger microscopy. The CoS_2-based film has a wrinkled surface, which appears relatively unchanged after an electrochemical durability test, while the NiS_2-like film preferentially loses Ni and the $(Co,Ni)S_2$-like film (based on nanoparticles with approximate composition $Co_{0.6}Ni_{0.4}S_2$) undergoes a phase separation (spinodal decomposition). All these films show an excess of S in the as-prepared form and after electrochemistry; evidence is presented for the possible presence of some polysulfides.

1. Introduction

The proton exchange membrane (PEM) fuel cell provides a promising alternative for future non-polluting vehicle propulsion and energy conversion devices due to its low greenhouse gas emissions, high efficiency and high energy density [1–3]. However, the commercialization of PEM fuel cells for automobile use depends on many factors, including cheaper catalysts for which Pt or Pt-based alloys are presently used [1]. There are other challenges with Pt, such as slow kinetics for the oxygen reduction reaction (ORR) and increasing dissolution as the catalyst particles become smaller [4,5]. Such challenges provide a motivation for investigating cheaper materials that display appreciable catalytic activity for ORR in acidic media (set by the conventionally-used membrane electrolytes), as well as having a sufficiently high open circuit potential (OCP) for meeting PEM fuel cell requirements (e.g., greater than 0.8 V vs. reversible hydrogen electrode (RHE)). One direction for developing non-precious metal catalysts is provided by the use of transition metal chalcogenides, and there has been interest in Chevrel phase compounds formed by Ru, Mo and Se [6], although the involvement of Ru would not necessarily reduce the cost compared with Pt. The present work has its genesis in observations by Baresel et al. [7] that transition metal sulfides with spinel and pyrite structures can be active for ORR, although that was before the opportunities for PEM fuel cells were fully realized.

This paper focuses on reporting characterizations of model ORR catalysts formed especially by CoS_2- and $(Co,Ni)S_2$-based materials. The study involves thin films prepared by magnetron sputtering in order to have defined surface areas so that activities can reasonably be related to measured current densities, and to enable direct comparison with a Pt standard [8]. Electrochemical examinations for ORR catalytic activity and durability of the thin films were assessed by the rotating disk electrode (RDE) dynamic polarization and the chronopotentiometric approaches [9]. A key new observation is that the $(Co,Ni)S_2$ material can demonstrate an OCP and current density with a better approach to values for Pt, than have been obtained previously for a transition metal chalcogenide. That suggested the need to also characterize a comparable NiS_2-based thin film, which established that the OCP for $(Co,Ni)S_2$ is synergistically enhanced compared with performances of the individual

* Corresponding authors.
E-mail addresses: karm@chem.ubc.ca (K.A.R. Mitchell), stephen.campbell@ballard.com (S.A. Campbell).

0021-9517/$ – see front matter
doi:10.1016/j.jcat.2008.06.016

components alone. Comparative surface and bulk characterizations of these materials are reported using scanning Auger microscopy (SAM), X-ray photoelectron spectroscopy (XPS), atomic force microscopy (AFM), scanning electron microscopy (SEM), micro-Raman spectroscopy, high-resolution X-ray diffraction (XRD) and energy dispersive X-ray (EDX) spectroscopy.

2. Experimental

The thin films were deposited on to glassy-carbon substrates (Tokai Carbon), which had been machined and polished, as described previously, to give a working surface area of 1.23 cm^2 [8]. Thin films were deposited using a magnetron sputter coater system (Model V3T, Corona Vacuum Coaters Inc.) with a radio frequency (13.6 MHz) power supply that varied between 35 and 40 W during the sputtering processes [8,10]. Sputter targets for deposition of the CoS_2- and NiS_2-based thin films were prepared using commercial CoS_2 (99.5% Alfa Aesar) and NiS_2 (99.5% Alfa Aesar) respectively, while that for the (Co,Ni)S_2-based film used a well-ground mixture of equal weights of the two commercial samples; each target was prepared by cold-pressing with approximately 20% by weight of S powder (99.98% Sigma Aldrich). The Pt thin film was prepared using direct current (dc) sputtering from a target prepared from Pt foil (99.95% Goodfellow).

Prior to each deposition, the coater system was turbomolecular pumped to its base pressure of 3.5×10^{-5} Torr. The plasma discharge was operated at 3.5×10^{-3} Torr with a continuous throttled flow of Ar (99.9% purity). To aid the film deposition, a bias of −180 V was applied to the substrate for the first minute of each deposition, and this was reduced to −75 V for the rest of the deposition process. Deposition times were adjusted to give film thicknesses of about 150 nm.

The electrochemical dynamical polarization measurements were performed using a jacketed three-compartment electrochemical cell, RDE rotator (Pine Instruments) and potentiostat (Autolab) as described previously [8]. The electrolytes were O_2-free and O_2-saturated 0.1 M $HClO_4$ (Fisher A.C.S.), and for the RDE experiments the rotation speed was varied from 400 to 2500 rpm. Prior to each experiment, electrolyte cleanliness was assessed by comparing the cyclic voltammogram (CV) measured with a standard Pt RDE (diameter 3 mm, Metrohm) against reference CVs [11,12]. The potential of the reversible hydrogen electrode (RHE) was checked by measuring the onset potential of H_2 evolution in the CV of the Pt RDE, and by measuring the potential difference against a commercial Hg|$HgSO_4$ reference electrode (AMEL). The CoS_2-, NiS_2- and (Co,Ni)S_2-based electrodes, as well as that for the Pt thin film, were mounted on an interchangeable RDE holder; this was specially designed to accommodate the top-hat-shaped glassy-carbon substrate on which the films were deposited, and to enable sample transfer between the electrochemical and surface analysis systems immediately after each experiment. The chronopotentiometric measurements gave an assessment of relative stability by monitoring change in potential with time for a fixed current (unique for each system), chosen such that the initial potential was 0.6 V. Note: this potential, and all subsequently quoted in this paper, are relative to the reversible hydrogen electrode (RHE).

Characterizations by SAM and XPS were respectively made with the Thermo Electron Microlab 350 and Leybold MAX200 systems described previously [8]. Surface topographies were imaged by AFM (Molecular Imaging) in the contact mode employing a Si_3N_4 cantilever. High-resolution X-ray diffraction (HRXRD) data were collected with a Philips X'Pert (PW 3040) diffractometer (Cu$K_{\alpha 1}$ source, resolution 0.01°) over the range 2–45° θ–θ with a scanning rate of 0.01° s^{-1}; before each measurement the diffractometer was calibrated using the standard Si wafer provided by the equipment manufacturer. Micro-Raman spectra were acquired with an inVia Raman Microscope (Renishaw) with HeNe laser (632.8 nm) and 50× objective (N.A. 0.75), following details described previously [13]. EDX spectra were measured with a Thermo Noran liquid N_2-cooled detector attached to the Microlab 350 facility (incident electron beam 15 keV).

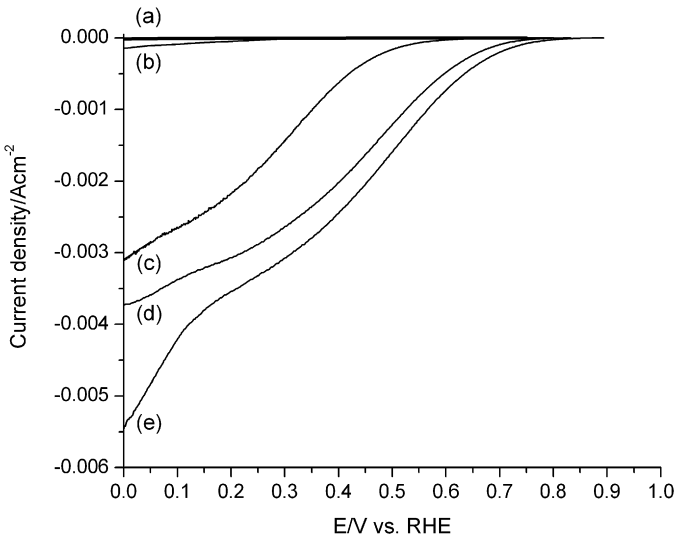

Fig. 1. Comparison of cathodic voltammograms for three thin films in 0.1 M $HClO_4$ solutions. The solutions are O_2-free for: (a) CoS_2 and (Co,Ni)S_2 (cannot distinguish at the scale shown) and (b) NiS_2; and O_2-saturated for: (c) NiS_2, (d) CoS_2 and (e) (Co,Ni)S_2. In each case the rotation rate is 2000 rpm and scan rate 5 mV s^{-1}.

3. Results and discussion

3.1. Electrochemical characterizations

The catalytic nature of CoS_2-, NiS_2- and (Co,Ni)S_2-based thin films for ORR was examined by slow scan voltammetry with rotation. Fig. 1 compares measurements of cathodic current-potential (I–V) curves obtained in O_2-free and O_2-saturated 0.1 M $HClO_4$ solutions. For all these thin films, larger cathodic currents are demonstrated in the O_2-saturated solution compared with the O_2-free solution, indicating an activity towards ORR. The OCP values in O_2-free solution are 0.74 V, 0.60 V and 0.75 V for CoS_2-, NiS_2- and (Co,Ni)S_2-based films, respectively, while the corresponding values in O_2-saturated solution are all larger and equal to 0.82 V, 0.80 V and 0.89 V, respectively. At any given potential for the O_2-saturated solution, the cathodic current density decreases in the order (Co,Ni)S_2 > CoS_2 > NiS_2.

Fig. 2 compares Tafel plots obtained using RDE for these three thin films in O_2-saturated 0.1 M $HClO_4$ solution, after making mass-transfer corrections, and direct comparisons are shown with that for the Pt thin film. In each case, the I–V curve was first scanned from 50 mV positive to OCP then swept cathodically to 0 V vs. RHE. From the Tafel plots in Fig. 2 for the sulfide-based films it can be seen that the OCP, and the ORR current at 0.8 V vs. RHE, are largest for the sample of (Co,Ni)S_2-type. Even so the activity for the latter is still 1.5–2 orders of magnitude lower than a sputtered Pt thin film, although it is around an order of magnitude better than for other transition metal chalcogenide catalysts investigated to date. All four curves appear to approach a common diffusion-limited current density at potentials more negative than 0.1 V.

Among the three sulfide-based thin-film catalysts investigated, the (Co,Ni)S_2 sample clearly has both the highest OCP, and the largest increase in current in O_2-saturated 0.1 M $HClO_4$ compared

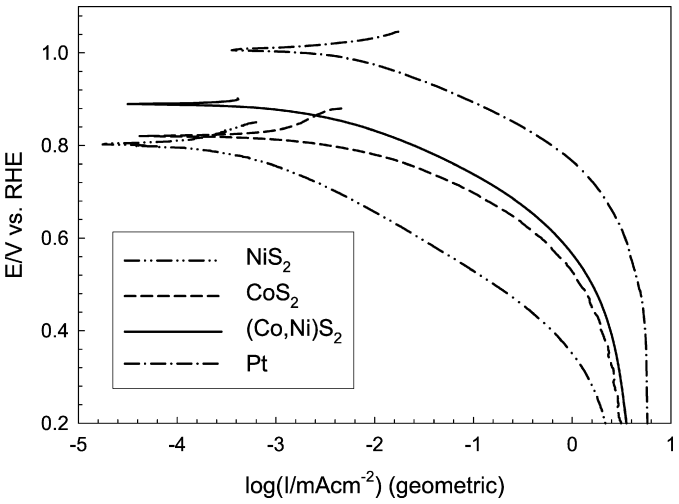

Fig. 2. Comparison of Tafel plots of dynamic polarization measurements in O_2-saturated 0.1 M $HClO_4$ for sputtered thin films formed by NiS_2, CoS_2, $(Co,Ni)S_2$ and Pt. In each case the rotation rate is 2000 rpm and scan rate 5 mV s^{-1}.

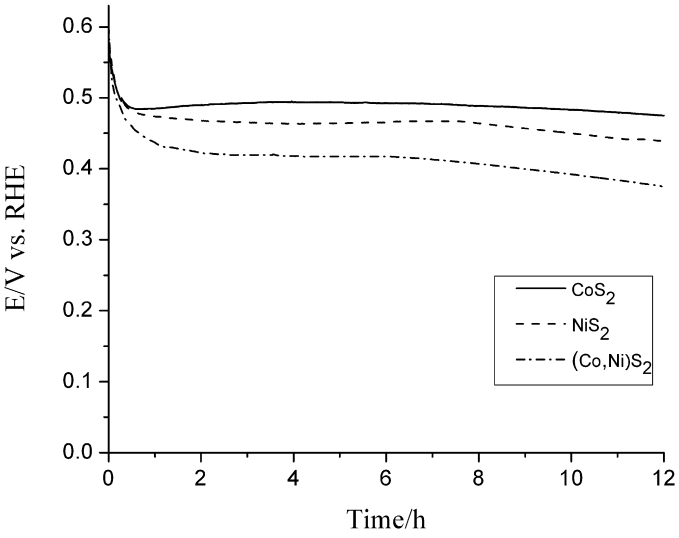

Fig. 3. Chronopotentiometric potential vs. time plots at constant current (see text) to show durability of CoS_2, NiS_2 and $(Co,Ni)S_2$ thin films in O_2-saturated 0.1 M $HClO_4$ solution. In each case the rotation rate is 2000 rpm and scan rate 5 mV s^{-1}.

with when each film is separately measured in the O_2-free electrolyte. The addition of NiS_2 to CoS_2 appears to have a synergistic effect in relation to ORR compared with the individual compound components. This highlights the need to characterize these materials more closely with regard to both bulk and surface properties, and work along these lines is described below. Furthermore, stability in acidic environments is another important aspect of electrochemical characterization.

Fig. 3 reports chronopotentiometry results for the three sulfide-containing thin films. For each film the current at 0.6 V, taken from the polarization measurement, was applied to the electrode in O_2-saturated electrolyte for 12 h, while potential was monitored. For all three films, after an initial drop in the first 20 min, no significant decrease was observed, indicating that all three films remained active over the 12 h period. The magnitude of the initial drop is greatest for the $(Co,Ni)S_2$-based film, which possibly relates to the phase separation phenomenon reported in Section 3.3.2 below.

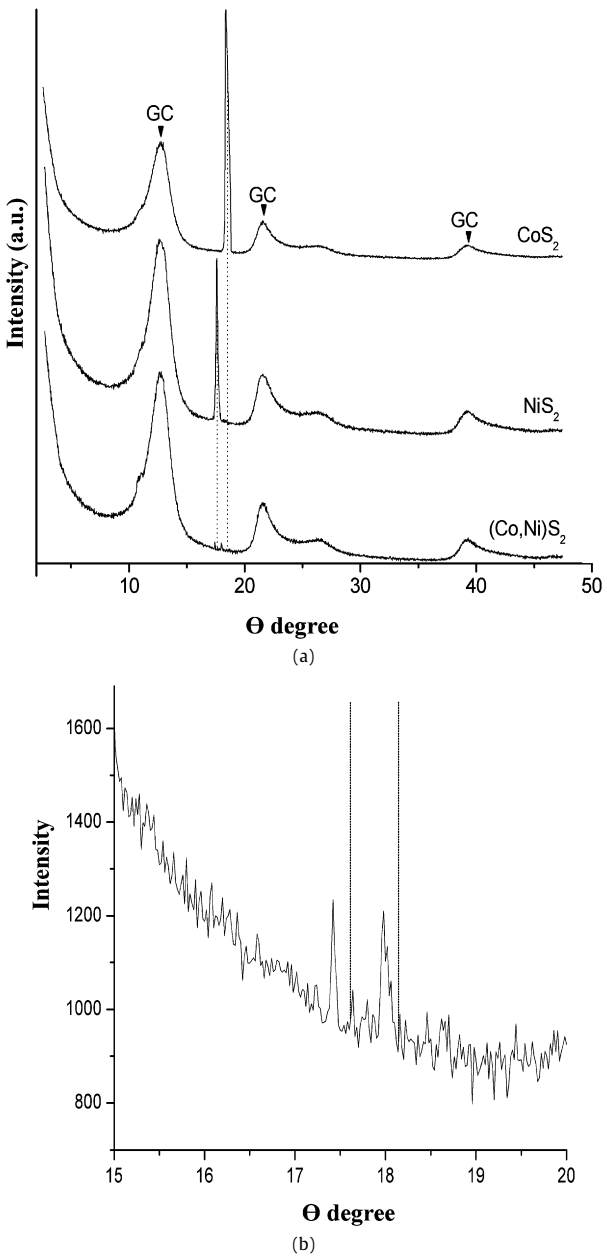

Fig. 4. (a) High-resolution X-ray diffractograms measured for the CoS_2, NiS_2 and $(Co,Ni)S_2$ thin films after the electrochemical measurements, where peaks associated with the glassy carbon are marked GC; and (b) a higher-magnification section for the $(Co,Ni)S_2$ film, where the vertical lines identify positions of peaks for the CoS_2 and NiS_2 films as in (a).

3.2. Bulk characterization of thin films after electrochemical characterization

3.2.1. XRD measurements

High-resolution X-ray diffractograms measured for the CoS_2-, NiS_2- and $(Co,Ni)S_2$-based thin films after electrochemical measurements are shown in Fig. 4a. Some broader peaks seen are associated with glassy carbon (marked GC), but the characteristic peaks located at $\theta = 18.13°$ in the CoS_2 pattern and at $\theta = 17.60°$ in the NiS_2 pattern are in good agreement with the (210) peaks for bulk CoS_2 [14] and bulk NiS_2 [15] respectively (the (210) orientation is often preferred for such films prepared by sputtering). By applying the Scherrer equation [16] to the characteristic peaks of the CoS_2 and NiS_2 thin films, the average particle sizes were estimated to be about 25 and 34 nm, respectively. An additional structure, compris-

ing of a shoulder near $\theta = 11.0°$, is detected in the diffractograms measured for all three thin-film samples, and this could indicate the presence of elemental S and/or anionic polysulfide species [17].

The XRD pattern obtained from the $(Co,Ni)S_2$ thin-film sample shows two small peaks at $\theta = 17.41°$ and 17.96°, and hence differences from the characteristic peaks for the CoS_2 and NiS_2 thin films (identified by the dashed vertical lines shown in both parts of Fig. 4). An examination using an XRD simulation package (Powdercell, Powder Cell for Windows, Version 2.4, Federal Institute for Materials Research and Testing, Germany) excluded the two small peaks observed for the $(Co,Ni)S_2$ thin film as arising from elemental components (formed by Co, Ni or S) or from binary compounds formed by Co and S, or by Ni and S. On the other hand, these small peaks (Fig. 4b) are within the fingerprint region identified for recognizing a $(Co,Ni)S_2$ solid solution [18,19]. These low-intensity peaks indicate that the $(Co,Ni)S_2$-like film has low crystallinity compared with the CoS_2- and NiS_2-based thin films, although the Scherrer equation applied to these peaks suggests that the contributing particles have an average dimension around 40 nm. Such nanocrystallites are likely interspersed within an amorphous matrix as observed for a related material formed by magnetron sputtering from Co and Se [10].

The peak at $\theta = 17.96°$ is positioned between the (210) peaks of CoS_2 and NiS_2 (both have the pyrite structure), which could be consistent with the (210) peak from a $(Co,Ni)S_2$ solid solution (this possibility may be supported by the Co–Ni–S phase diagram [20], although no heating was done during the fabrication process to equilibrate the system). That hypothesis was pursued according to the following discussion. Assuming that the experimental peak at $\theta = 17.96°$ originates with reflections from the (210) planes of a pyrite structure, the lattice constant is established to be 5.5860 Å, a value that can be compared with the two parent lattice constants (5.5350 Å for CoS_2 [14] and 5.6700 Å for NiS_2 [15]). If the family with formula $Co_xNi_{1-x}S_2$ maintains a linear relation between x and lattice constant (i.e. the ideal Vegard's law [21]), then x is estimated to be about 0.6 for our sample, and consistently Bouchard et al. reported the value of the lattice constant for $Co_{0.6}Ni_{0.4}S_2$ to equal 5.5861 ± 0.0005 Å [18]. This supports the presence of a $(Co,Ni)S_2$ solid solution in the thin film, although background data remain lacking for identifying the origin of the small experimental peak at $\theta = 17.41°$.

3.2.2. Raman characterization

For Raman measurements, the commercial CoS_2 and NiS_2 samples used for making the sputtering targets (Section 2) were used as standards. The Raman spectrum from the commercial CoS_2 powder showed characteristic peaks at 287 and 389 cm^{-1} as well as structure around 410 cm^{-1} (Fig. 5). This is in close agreement with a literature report for CoS_2 single crystal [22], with the additional possibility that the peak at 287 cm^{-1} may also be associated with polysulfides [23]. In contrast, the Raman spectrum obtained from the magnetron-sputtered thin film formed from CoS_2 shows a pronounced peak at 391 cm^{-1}, a broad shoulder at around 410 cm^{-1} and a peak at 287 cm^{-1}, with a general similarity to the spectrum obtained from the CoS_2 standard. However, there is peak broadening for the thin film, which appears to relate to disorder effects [24], since the film was not annealed. According to literature reports, Raman spectra from polysulfides typically exhibit a characteristic peak in the range 460–470 cm^{-1}, though other much weaker peaks at about 425, 260–275 and 280–290 cm^{-1} have also been reported [23]. The CoS_2-based film does show Raman features at 460–470 cm^{-1}, as well as at 287 cm^{-1}, both of which can be attributed to polysulfides (although the latter feature is also characteristic of the CoS_2 standard). The Raman spectrum of commercial NiS_2 (Fig. 5) shows distinctive peaks at 282 and 477 cm^{-1}, and a shoulder at 488 cm^{-1}. This spectrum is in good agreement

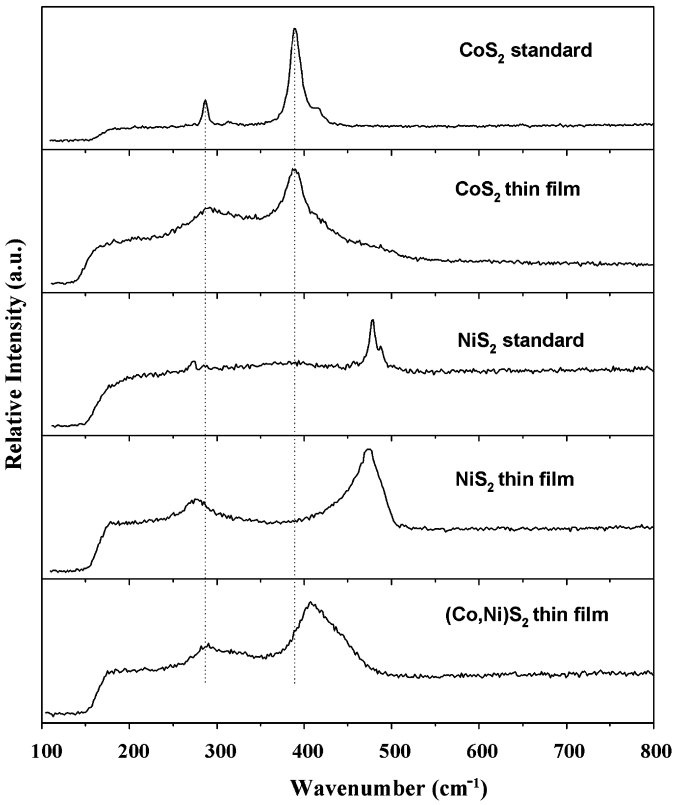

Fig. 5. Raman spectra measured with HeNe laser for the CoS_2, NiS_2 and $(Co,Ni)S_2$ thin films and compared with those measured for standard CoS_2 and NiS_2 samples.

with measurements made for NiS_2 single crystals [22,25]. The Raman spectrum of the NiS_2-based thin film has an asymmetric peak at 475 cm^{-1} with a shoulder out to 484 cm^{-1} and a small broad peak at 275–288 cm^{-1}, suggesting that the thin film contains the primary Raman scattering features observed in the NiS_2 standard. However, the asymmetric shoulder below 475 cm^{-1} is new and overlaps the region where polysulfides are expected.

The Raman spectrum from the $(Co,Ni)S_2$-based thin film is different from a simple combination of Raman spectra obtained from the CoS_2 and NiS_2 types of film. The main Raman peak of $(Co,Ni)S_2$ is centered at 409 cm^{-1}, and between those of the CoS_2-based (391 cm^{-1}) and NiS_2-based (477 cm^{-1}) thin films. There is no evidence in the spectrum for the $(Co,Ni)S_2$ film of significant contributions by peaks at either 391 cm^{-1} or 477 cm^{-1}, although some contribution at the former position could be obscured by the broadening seen in that spectrum. Overall the peak broadening and shift in the main Raman peak for the $(Co,Ni)S_2$-based film are consistent with that film being amorphous and involving solid solution formation [21,24], and the latter conclusion is fully consistent with the spectrum measured for a $Co_{0.9}Ni_{0.1}S_2$ single crystal [22]. The broad shoulder of the peak at 409 cm^{-1} overlaps the region (460–470 cm^{-1}) where Raman transitions for polysulfides are characteristically expected.

In principle elemental S could also be present at the surfaces of these thin films. Raman spectra of different allotropes of solid elemental S typically have intense peaks within the region 400–500 cm^{-1} and multiple intense peaks below 300 cm^{-1} [23]. Among the more established Raman spectra of solid allotropes are S_8 with major Raman peaks at 151, 221 and 474 cm^{-1}, as well as S_6 with strong Raman peaks at 202, 262, 448 and 471 cm^{-1} [23,26]. However, Fig. 5 shows no evidence for these, so suggesting that, according to the Raman analysis, elemental S is not present significantly on any of the thin films studied here, though the presence of polysulfides cannot be ruled out.

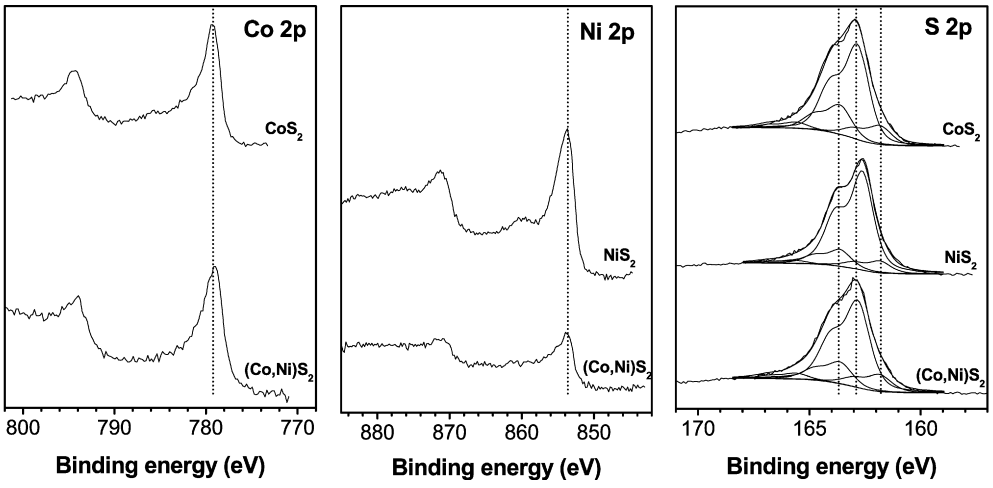

Fig. 6. Co 2p, Ni 2p and S 2p spectra measured from the CoS_2, NiS_2 and $(Co,Ni)S_2$ thin films. See text for details of curve fitting for the S 2p spectra.

3.3. Thin film surface characterization

3.3.1. XPS analysis after ORR activity measurement

The sputtered CoS_2-, NiS_2- and $(Co,Ni)S_2$-based thin films were characterized by XPS after ORR activity assessment. XPS showed their surface regions to be S-rich (with sulfur-to-metal (S/M) atomic ratios equal to 6.0, 3.5 and 3.8, respectively). The measured Co 2p, Ni 2p and S 2p spectra for these thin films are reported in Fig. 6. For the CoS_2-based film, the Co 2p photoemission peak shows a single Co $2p_{3/2}$ chemical state at 779.2 eV, whereas the breadth of the S 2p peak reveals the presence of more than one chemical state, although the dominant structure corresponds to a S $2p_{3/2}$ component with a binding energy of 162.9 eV. These values can be compared with the binding energies of 778.1 and 162.6 eV for Co $2p_{3/2}$ and S $2p_{3/2}$ respectively reported for a CoS_2 single crystal [27]. Some conclusions for surfaces of the CoS_2-based thin film are: (i) contributions from elemental S are small or non-existent (the expected S $2p_{3/2}$ binding energy is around 164.0 eV [28]); (ii) the majority of S atoms exist in a S_2^{2-}-like chemical state; and (iii) the Co atoms experience an increased electronegative environment compared to those atoms within the CoS_2 single crystal (suggested by the shift of 1.1 eV to higher binding energy for Co $2p_{3/2}$ in the film).

The binding energies for the XPS peaks from the NiS_2-based film (Ni $2p_{3/2}$ 853.7 eV, S 2p 162.6 eV) are close to the values reported for single-crystal NiS_2 (Ni $2p_{3/2}$ 853.6 eV, S 2p 162.7 eV) [25,27], supporting the conclusion that this film is similar to NiS_2 with the pyrite structure. For the $(Co,Ni)S_2$-based thin film, Fig. 6 shows that the Co $2p_{3/2}$ and Ni $2p_{3/2}$ peak positions line up quite well with those of the CoS_2- and NiS_2-based films, although its S 2p structure is centered at 162.9 eV, as for the CoS_2-based film.

In summary, these measurements suggest a single chemical state for Co and for Ni [28,29], but some variation is observed for the S state. Curve fitting for the latter case is difficult in the absence of appropriate standards, but our previous experience with FeS_2 (both thin film and mineral samples) may be useful [30]. That work for S 2p showed one could use $2p_{3/2}$ components at the following binding energies: 161.8 eV for S_2^{2-} ions (surface) with less than the full Fe coordination [31], 162.6 eV for S_2^{2-} ions in the bulk [32–35], and 163.6 eV for short-chain polysulfides (S_n^{2-}, $2 < n < 8$) [36], supplemented by a broad component at 165.6 eV associated with energy loss processes [31,36]. The components for fitting the S 2p spectra in Fig. 6 used the same binding energies, except the value for bulk S_2^{2-} was allowed to vary from that of FeS_2 (162.6 eV) (the optimized values turned out to be 162.6 eV for the NiS_2-based film and 162.8 eV for both those related to CoS_2 and $(Co,Ni)S_2$). The relative proportions of the three components representing different chemical states for the sulfide-based thin films are summarized in Table 1 (the comparable values for the FeS_2-like thin film after electrochemistry were reported to be 85% bulk S_2^{2-}, 8% surface S_2^{2-} and 7% polysulfides [30]). Sulfate with a binding energy ~168 eV or more [28] is not detected at the surfaces of these thin films.

Table 1
Percentages for different components indicated by curve fitting of S 2p spectra for the CoS_2-, NiS_2- and $(Co,Ni)S_2$-based thin films after electrochemistry

	S^{2-} (surf)	S^{2-} (bulk)	poly-S
CoS_2	21	66	13
NiS_2	13	78	9
$(Co,Ni)S_2$	17	70	13

3.3.2. Characterization after the durability test

Fig. 7 shows scanning electron micrographs for the three thin films before and after the durability test, which was applied after the original ORR electrochemical assessment and its associated surface characterization. Fig. 7a shows that CoS_2 has a wrinkled surface. This structure remains unchanged after ORR measurements as well as after the durability test (Fig. 7b), which indicates considerable film stability in the acidic environment. Such morphologies have been reported previously for magnetron sputtered W and Ti oxysulfide thin films [37,38]; this form is believed to be associated with stress relaxation in film formation, particularly where one component has an enhanced mobility [39]. The wrinkled morphology in the present work appears associated with the high S content at the surface. Fig. 8 shows a more-detailed image taken by atomic force microscopy (AFM) for the CoS_2 sample, including a profile scan. The heights of the wrinkles are around 80–100 nm, while their widths are consistently about 150 nm; the root-mean-square roughness is estimated at 30 nm. Fig. 9a compares Auger spectra measured across a selected film area after the ORR analysis and following the durability test. Both spectra indicate the presence of Co and S, as well as a KLL signal associated with adventitious C from handling and a trace signal from O. There is no significant change in surface composition after the durability test, supporting the conclusion for the stability of the CoS_2-like film in the acidic solution. In addition to the area analysis, multiple Auger point measurements confirmed that the surface compositions are essentially constant in the valleys, tops and sides of the wrinkles, and that they do not change upon electrochemical testing.

The morphology of the as-prepared NiS_2 film (Fig. 7c) is smooth and similar to the surface of the underlying glassy–carbon sub-

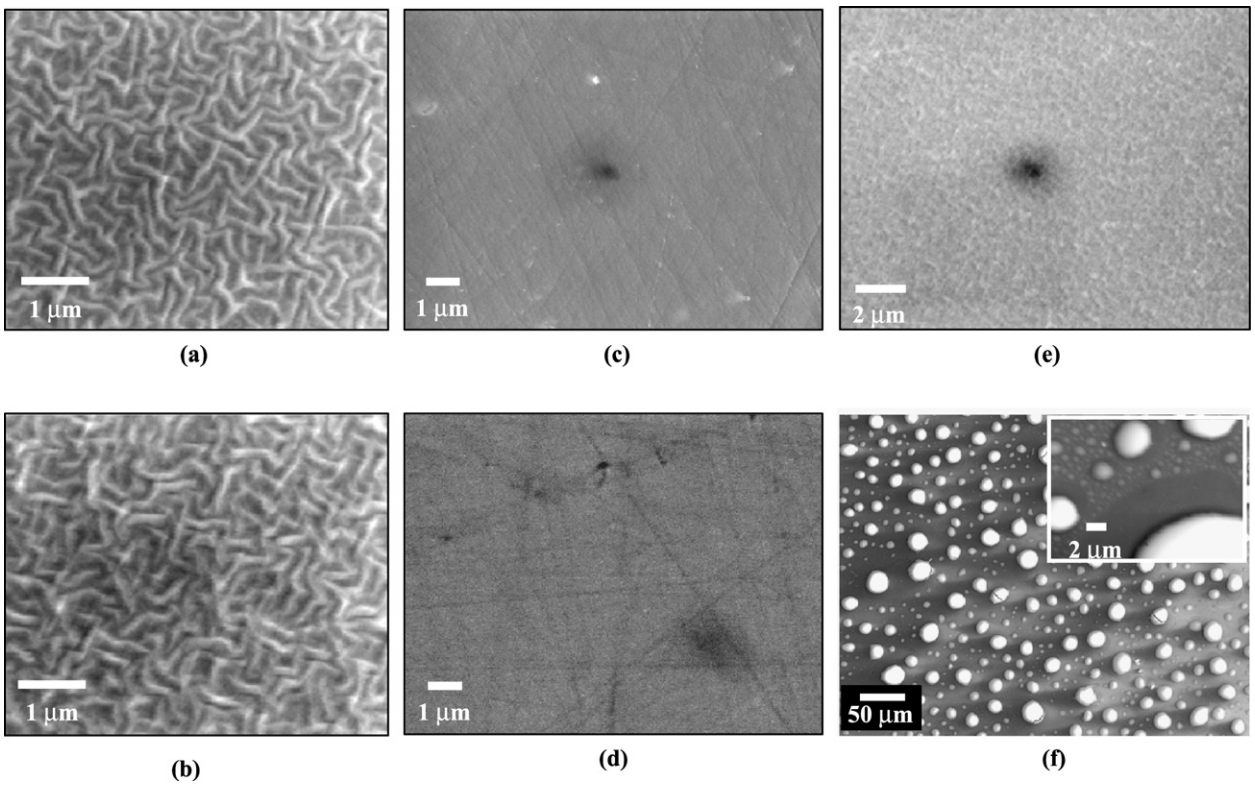

Fig. 7. Scanning electron micrographs measured from three thin films: (a) CoS_2, (c) NiS_2 and (e) $(Co,Ni)S_2$ all before the electrochemical durability test; and (b) CoS_2, (d) NiS_2 and (f) $(Co,Ni)S_2$ all after the durability test.

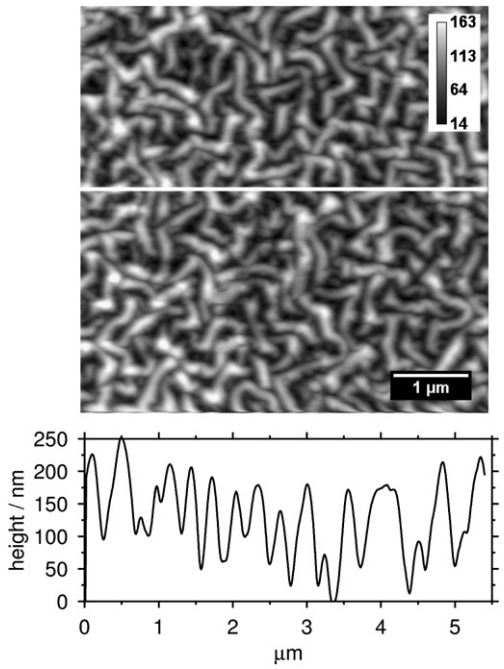

Fig. 8. AFM topographical image of the wrinkled surface of the CoS_2 thin film with profile for the line scan taken along the horizontal line shown in the image.

strate. Although Auger spectra taken from the film after ORR and following the durability test are similar (Fig. 9b), the SEM micrograph after the durability test (Fig. 7d) shows more polishing scratches from the underlying substrate. That suggests some thinning of the film upon dissolution, although the stripping appears to be uniform.

The surface of the as-prepared $(Co,Ni)S_2$ film (Fig. 7e) is relatively flat with much finer wrinkled features than the CoS_2 film. The morphology of this film remains unchanged after the ORR analysis, but, following the durability test (chronopotentiometric measurement), spherical (ball-like) features form on its surface (Fig. 7f). Surface compositions measured from these micro-regions using SAM have been compared to those before the durability test (Fig. 9c). The $(Co,Ni)S_2$ thin film after ORR analysis shows a uniform surface composed of Co, Ni and S, with no O, but there is also adventitious C from handling. However, after the durability test, the off-sphere region contains Co, S, traces of O, and a larger C signal. The non-detection of Ni indicates that this element has been depleted from this region, whereas Auger spectra from the ball region indicate the presence of Co, Ni and O, with only a trace of S and C. The difference in intensity of the C signal from the two adjacent sites (i.e. on and off the sphere) indicates that the film between the spheres became sufficiently thin for the underlying glassy carbon to be detected by Auger electron spectroscopy. By contrast, only a trace of C is detected from the sphere, due to its diameter being larger than the Auger probe depth. The Co and Ni Auger signals from the ball region have shifted to lower kinetic energies compared with the initial state, consistently with the formation of metal oxide. This surface oxidation has occurred in the absence of appreciable S, so suggesting that in the as-prepared state, where oxidation is not apparent, S acts to passivate the surface.

EDX point measurements taken from the off-ball regions do not detect Ni, so providing an independent confirmation that element has been removed from those areas during the electrochemical durability test. Measurements by EDX from the ball region (Fig. 10) confirm the presence of Co, Ni and S within the bulk, although the Auger analysis emphasizes that the surface is modified. In summary, both compositional and morphological changes observed for the $(Co,Ni)S_2$-like thin film indicate that the electrochemical durability test causes a separation into two phases. Such a process is commonly referred to as spinodal decomposition [40].

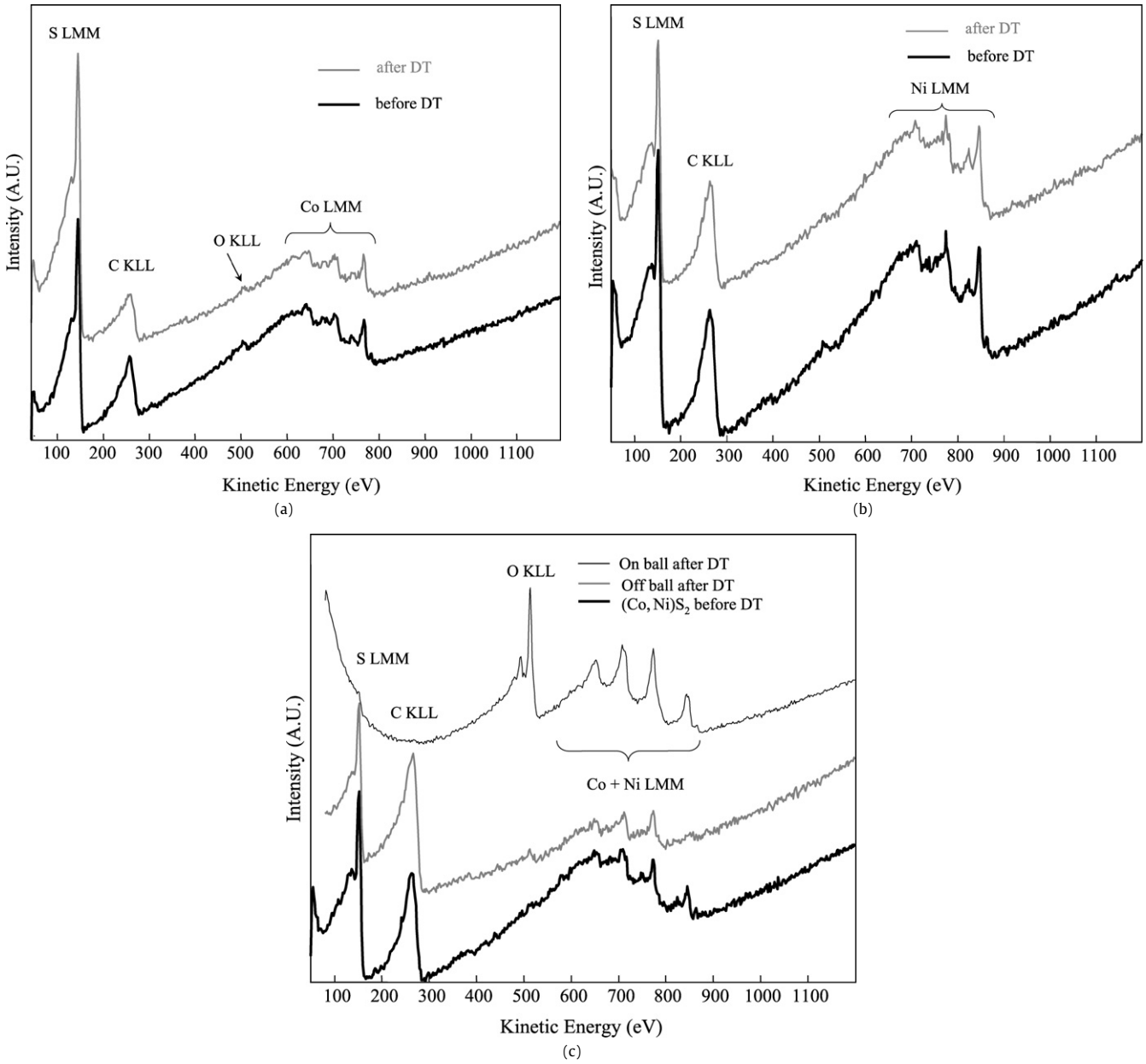

Fig. 9. Auger electron spectra measured before and after electrochemical durability test (DT) for: (a) CoS_2, (b) NiS_2 and (c) $(Co,Ni)S_2$ thin films. In (c), spectra measured after the durability test are compared from on and off the spheres shown in Fig. 7f.

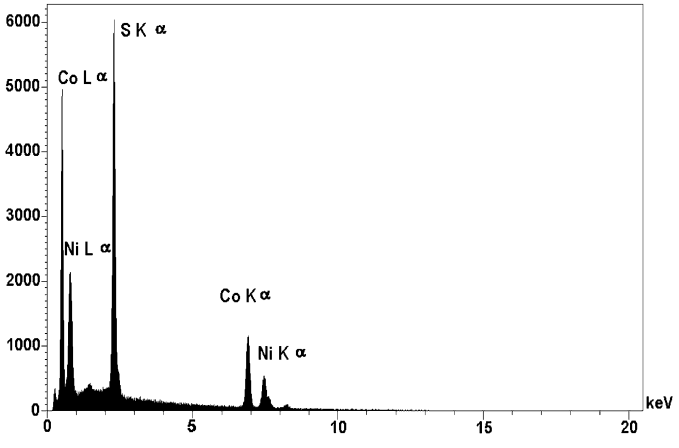

Fig. 10. EDX spectrum measured from a sphere on the surface of the $(Co,Ni)S_2$ thin film after the durability test.

3.4. Overview

The comparison of the OCP and ORR current densities measured for the CoS_2- and NiS_2-based thin films, with those of the corresponding pure crystalline disulfide materials reported in the literature [7], indicate higher ORR catalytic activity for the thin films. However, the latter are different insofar as they are composed of metal disulfide nanoparticles and the S-rich surfaces include a variety of chemical states. Such differences appear intrinsically related to the magnetron sputtering method used for fabricating the films. This is consistent with differences already observed between mineral samples of FeS_2 and those prepared by magnetron sputtering. The latter showed higher OCP and higher current density, as well as an independent indication that polysulfides are present from the sample preparation [30].

The ternary catalyst $(Co,Ni)S_2$ in the form of a thin film shows an improvement in ORR catalytic activity compared with the films of CoS_2- and NiS_2-types, with the improvement amounting to

70 mV in the OCP and by a factor of 10 for current density at 0.8 V (e.g. Fig. 2). The evidence from XRD and Raman spectroscopy suggests that the synergistic effect from adding NiS_2 to CoS_2 results in solid solution formation, for which new physical and chemical properties may be expected [41]. Other factors that have been proposed for such effects include nanoparticle size and the introduction of a different crystal structure [42]. Nanoparticle size may be a factor with the $(Co,Ni)S_2$-like thin film, since we may not be able to distinguish very small particles from amorphous regions, but XRD from the nanocrystallites is consistent with maintaining the pyrite structure.

Another factor concerns electronic structure. While geometrically both bulk CoS_2 and NiS_2 have the pyrite structure, their electronic characteristics are different insofar as the first has been described as a half-metal ferromagnet [43], while the second is a Mott insulator [44]. Further differences may be expected with alloying, but their effects on ORR remain unknown, although more understanding would likely follow from new theoretical studies (e.g. for the interaction of O_2 with mixed disulfides).

As well as the effect on electronic structure for the alloying of NiS_2 with CoS_2, another interesting question concerns the role of S enrichment at the surfaces. It can be concluded from the electrochemical tests made here that these thin films with S-rich surfaces are sufficiently conductive (unlike elemental S) to facilitate electron transfer for ORR, but the mechanisms involved remain unknown, including the nature of the active sites, the role of polysulfides, and whether the electron transfer primarily occurs through bonds or through-space tunneling [45–47].

4. Concluding remarks

Since the early 1840s, when Grove and Schoenbein first presented the acid fuel cell [48], platinum has been the catalyst of choice. Developing commercially viable fuel cells, however, has been hampered by the scarcity, and hence the price, of this precious noble metal. We investigated materials formed from disulfides of cobalt and nickel as lower-cost alternatives to Pt for oxygen reduction. It has been demonstrated that the ORR activity decreases as $(Co,Ni)S_2 > CoS_2 > NiS_2$ for sputtered thin films on glassy carbon substrates. Characterization of these films with XRD indicates that they are nanocrystalline with a pyrite structure, and that the mixed-metal film involves a solid solution, probably with some amorphous material. Raman spectroscopy supports these conclusions and suggests the presence of some polysulfide, apparently as a result of the sputtering process. XPS and Auger electron spectroscopy show that each metal is in a single chemical state, and that there is no detectable elemental sulfur even though the surfaces are S-rich. These surfaces do not appear to bind oxygen tightly, but they maintain sufficient electronic conductivity to remain active without the passivation that can occur with an insulating oxide on a metal. While the film formed from CoS_2 is stable for several hours under O_2 reduction conditions, the mixed-metal film degraded, apparently as a consequence of the spinodal decomposition observed. Nevertheless the activity observed for ORR suggests that chalcogenide materials may yet provide a fertile field for investigation in this context.

Acknowledgments

This research was supported jointly by Ballard Power Systems and by the United States Department of Energy under contract DE-FC36-03GO13107. The authors acknowledge the help and advice of Ms. A. Lam, Dr. B. Patrick, Dr. I.C. Robin and Ms. A. Sode, and thank the Natural Sciences and Engineering Research Council of Canada for support to M. Teo.

References

[1] H.A. Gasteiger, S.S. Kocha, B. Sompalli, F.T. Wagner, Appl. Catal. B 56 (2005) 9.
[2] D.S. Cameron, Platinum Met. Rev. 49 (2005) 16.
[3] D. Hart, J. Power Sources 86 (2000) 23.
[4] R. Adzic, in: J. Lipkowski, P.N. Ross (Eds.), Electrocatalysis, Wiley–VCH, New York, 1998, p. 197.
[5] W. Bi, G.E. Gray, G.E. Fuller, Electrochem. Solid State Lett. 10 (2007) B101.
[6] N. Alonso-Vante, H. Tributsch, Nature 323 (1986) 431.
[7] V.D. Baresel, W. Sarholz, P. Scharner, J. Schmitz, Ber. Bunsen-Ges. Phys. Chem. 78 (1974) 608.
[8] D. Susac, A. Sode, L. Zhu, P.C. Wong, M. Teo, D. Bizzotto, K.A.R. Mitchell, R.R. Parsons, S.A. Campbell, J. Phys. Chem. B 110 (2006) 10762.
[9] A.J. Bard, L.R. Faulkner, Electrochemical Methods: Fundamentals and Applications, Wiley, New York, 2001.
[10] L. Zhu, D. Susac, P.C. Wong, M. Teo, S.A. Campbell, D. Bizzotto, R.R. Parsons, K.A.R. Mitchell, J. Solid State Chem. 179 (2006) 3942.
[11] J. Clavilier, R. Faure, G. Guinet, R. Durand, J. Electroanal. Chem. 107 (1980) 205.
[12] V. Stamenkovic, N.M. Markovic, P.N. Ross, J. Electroanal. Chem. 500 (2001) 44.
[13] M. Teo, P.C. Wong, L. Zhu, D. Susac, S.A. Campbell, D. Bizzotto, R.R. Parsons, K.A.R. Mitchell, Appl. Surf. Sci. 253 (2006) 1130.
[14] International Center for Diffraction Database, PDF 03-065-3322 (CoS_2).
[15] International Center for Diffraction Database, PDF 00-011-0099 (NiS_2).
[16] B.D. Cullity, Elements of X-ray Diffraction, Addison–Wesley, Reading, MA, 1978.
[17] International Center for Diffraction Database, PDF 03-065-1436 (S_8); PDF 00-039-0826 ($Ga_{1.66}CrS_4$); PDF 01-078-2034 ($BaVS_3$); PDF 01-078-0792 (S_{11}); PDF 01-072-0409 (S_{18}); PDF 01-072-0410 (S_{20}).
[18] R.J. Bouchard, Mater. Res. Bull. 3 (1968) 563.
[19] O. Knop, C.H. Huang, K.I.G. Reid, J.S. Carlow, F.W.D. Woodhams, J. Solid State Chem. 16 (1976) 97.
[20] P. Villars, A. Prince, H. Okamoto (Eds.), Handbook of Ternary Alloy Phase Diagrams, ASM International, Materials Park, OH, 1995, pp. 8576–8578.
[21] A.R. West, Solid State Chemistry and Its Applications, Wiley–Interscience, New York, 1984.
[22] E. Anastassakis, C.H. Perry, J. Chem. Phys. 64 (1976) 3604, and references therein.
[23] B. Eckert, R. Steudel, Top. Curr. Chem. 231 (2003) 31.
[24] H. Bubert, H. Jentte, Surface and Thin Film Analysis: A Compendium of Principles, Instrumentation and Applications, Wiley–VCH, Weinheim, 2002.
[25] T. Suzuki, K. Uchinokura, T. Sekine, E. Matsuura, Solid State Commun. 23 (1977) 847.
[26] K. Nagata, T. Nishio, H. Taguchi, Y. Miyamoto, Jpn. J. Appl. Phys. 31 (1992) 1078.
[27] H. van der Heide, R. Hemmel, C.F. van Bruggen, C. Haas, J. Solid State Chem. 33 (1980) 17.
[28] J.F. Moulder, W.F. Stickle, P.E. Sobol, K.D. Bomben, Handbook of X-ray Photoelectron Spectroscopy, Physical Electronics Inc., Eden Prairie, MN, 1995.
[29] D. Briggs, M.P. Seah, Practical Surface Analysis, Wiley, New York, 1990.
[30] D. Susac, L. Zhu, M. Teo, A. Sode, K.C. Wong, P.C. Wong, R.R. Parsons, D. Bizzotto, K.A.R. Mitchell, S.A. Campbell, J. Phys. Chem. C 111 (2007) 18715.
[31] S. Karthe, R. Szargan, E. Suoninen, Appl. Surf. Sci. 72 (1993) 157.
[32] J.R. Mycroft, G.M. Bancroft, N.S. McIntyre, J.W. Lorimer, I.R. Hill, J. Electroanal. Chem. 292 (1990) 139.
[33] P. Bonnissel-Gissinger, M. Alnot, J.J. Ehrhardt, P. Behra, Environ. Sci. Technol. 32 (1998) 2839.
[34] H.W. Nesbitt, G.M. Bancroft, A.R. Pratt, M.J. Scaini, Am. Mineral. 83 (1998) 1067.
[35] S.L. Harmer, H.W. Nesbitt, Surf. Sci. 564 (2004) 335.
[36] I. Uhlig, R. Szargan, H.W. Nesbitt, K. Laajalehto, Appl. Surf. Sci. 179 (2001) 222.
[37] I. Marti-Litas, P. Vinatier, A. Levasseur, J.C. Dupin, D. Gonbeau, F. Weill, Thin Solid Films 416 (2002) 1.
[38] M.H. Lindic, H. Martinez, A. Benayad, B. Pecquenard, P. Vinatier, A. Levasseur, D. Gonbeau, Solid State Ionics 176 (2005) 1529.
[39] R. Huang, Z. Suo, J. Appl. Phys. 91 (2002) 1135, and references therein.
[40] P.F. Green, Kinetics, Transport, and Structure in Hard and Soft Materials, CRC Press, New York, 2005, pp. 267–291.
[41] T.A. Bitcher, R.J. Bouchard, W.H. Cloud, P.C. Donohue, W.J. Siemons, Inorg. Chem. 7 (1968) 2208.
[42] R.E. Smallman, R.J. Bishop, Metals and Materials: Science, Processes, Applications, Oxford Univ. Press, Boston, MA, 1995.
[43] R. Yamamoto, A. Machida, Y. Moritomo, A. Nakamura, Phys. Rev. B 59 (1999) R7793.
[44] A.K. Mabatah, E.J. Yoffa, P.C. Eklund, M.S. Dresselhaus, D. Adler, Phys. Rev. B 21 (1980) 1676.
[45] M.C. McCarthy, S. Thorwirth, C.A. Gottleib, P. Thaddeus, J. Chem. Phys. 121 (2004) 632.
[46] A.C. Benniston, A. Harriman, Chem. Soc. Rev. 35 (2006) 169.
[47] R.J.F. Dalrymple, W.E. Spear, J. Phys. Chem. Solids 33 (1972) 1071.
[48] G. Sandstede, E.J. Cairns, V.S. Bagotsky, K. Wiesener, in: V. Vielstich, H.A. Gasteiger, A. Lamm (Eds.), Handbook of Fuel Cells: Fundamental, Technology and Applications, vol. 1, Wiley, New York, 2003, p. 155.